

Differential reddening in the direction of 56 Galactic globular clusters

M. V. Legnardi¹★, A. P. Milone^{1,2}, G. Cordoni¹, E. P. Lagioia¹, E. Dondoglio¹, A. F. Marino^{2,3}, S. Jang⁴, A. Mohandasani¹, and T. Ziliotto¹

¹ *Dipartimento di Fisica e Astronomia “Galileo Galilei”, Univ. di Padova, Vicolo dell’Osservatorio 3, Padova, IT-35122*

² *Istituto Nazionale di Astrofisica - Osservatorio Astronomico di Padova, Vicolo dell’Osservatorio 5, Padova, IT-35122*

³ *Istituto Nazionale di Astrofisica - Osservatorio Astrofisico di Arcetri, Largo Enrico Fermi, 5, Firenze, IT-50125*

⁴ *Center for Galaxy Evolution Research and Department of Astronomy, Yonsei University, Seoul 03722, Korea*

Accepted 2023 April 05. Received 2023 April 04; in original form 2022 December 23

ABSTRACT

The presence of differential reddening in the direction of Galactic globular clusters (GCs) has proven to be a serious limitation in the traditional colour-magnitude diagram (CMD) analysis. Here, we estimate local reddening variations in the direction of 56 Galactic GCs. To do that, we use the public catalogs derived as part of the *Hubble Space Telescope* UV Legacy Survey of Galactic Globular Clusters, which include photometry in the F275W, F336W, F438W, F606W, and F814W filters. We correct photometry for differential reddening finding that for 21 out of 56 GCs the adopted correction procedure significantly improves the CMDs. Moreover, we measure the reddening law in the direction of these clusters finding that R_V exhibits a high level of variability within the Galaxy, ranging from ~ 2.0 to ~ 4.0 . The updated values of R_V have been used to improve the determination of local reddening variations and derive high-resolution reddening maps in the direction of the 21 highly-reddened targets within our sample. To compare the results of the different clusters, we compute the 68th percentile of the differential-reddening distribution, $\sigma_{\Delta A_{F814W}}$. This quantity ranges from 0.003 mag to 0.030 mag and exhibits a significant anti-correlation with the absolute module of the Galactic latitude and a strong correlation with the average reddening in the direction of each cluster. Therefore, highly-reddened GCs located in the proximity of the Galactic plane typically show higher differential-reddening variations across their field of view.

Key words: globular clusters: general, Hertzsprung–Russell and colour–magnitude diagrams, techniques: photometry

1 INTRODUCTION

Galactic globular clusters (GCs) are remarkable fossils from the early Universe. Being among the most ancient objects of the Galaxy, they provide unique insights into nucleosynthesis, star formation, and chemical enrichment at the earliest stages of the Galaxy’s formation. One of the most serious challenges in the study of many GCs, especially the ones in the direction of the Galactic Center, is the presence of spatially-variable extinction, better known as differential reddening, caused by variation of dust column density across the field of view (FoV). By introducing a significant broadening of all evolutionary sequences in colour-magnitude diagrams (CMDs), differential reddening complicates the traditional CMD analysis preventing an accurate determination of some fundamental parameters, such as age, distance, and metallicity (e.g. [Bonatto et al. 2013](#)). Moreover, differential reddening hinders the detection and characterization of the various stellar sequences that compose the CMDs, including binaries and multiple stellar populations in GCs (e.g. [Milone et al. 2012](#)). Therefore, correcting the photometry for the effects of differential reddening is a crucial step for a correct analysis of the CMD.

Over the years, several methods have been developed to model and correct for spatially variable extinction in the direction of Galactic GCs. A first approach consists of dividing the FoV across the cluster

in a regular cell grid, extracting the CMD of the stars included in each cell, and computing the differential reddening of each cell as the average colour distance, calculated across the reddening line, between the extracted CMD and the bluest ones (e.g. [Kaluzny & Krzeminski 1993](#); [Heitsch & Richtler 1999](#); [Piotto et al. 1999](#); [von Braun & Mateo 2001](#); [Sarajedini et al. 2007](#); [McWilliam & Zoccali 2010](#); [Gonzalez et al. 2011](#); [Bonatto et al. 2013](#)). An alternative method has been introduced by [Milone et al. \(2012\)](#) and then extensively used to investigate star clusters in the Milky Way and in Magellanic Clouds (e.g. [Lagioia et al. 2014](#); [Milone 2015](#); [Bellini et al. 2017](#); [Li et al. 2017](#); [Pallanca et al. 2021](#); [Dondoglio et al. 2022](#); [Legnardi et al. 2022](#)). In a nutshell, they estimated the differential reddening of each star in a cluster by defining a reference line for the upper main sequence (MS), the sub-giant branch (SGB), and the red-giant branch (RGB) and then calculating the colour distance of each cluster star from it along the reddening vector. The final differential-reddening value associated with each star corresponds to the median colour displacement of the spatially closest objects.

Recently, our group has undertaken an extensive investigation of differential reddening in the FoV of more than a hundred star clusters in the Magellanic Clouds by means of *Hubble Space Telescope* (HST) images ([Milone et al. 2022](#)). Moreover, we investigated reddening variations across the FoV of 43 Galactic GCs ([Jang et al. 2022](#)), based on ground-based wide-field photometry from [Stetson et al. \(2019\)](#). Here, we constrain the amount of differential reddening in

★ E-mail: mariavittoria.legnardi@phd.unipd.it

the central regions of 56 Galactic GCs by using high-precision *HST* photometry and astrometry by Nardiello et al. (2018).

Milone et al. (2012) and Bonatto et al. (2013) investigated local reddening variations across the FoV for a large sample of Galactic GCs (59 and 66, respectively) by using *HST* data. Both works are based on the data of the GO-10775 program alone (PI: A. Sarajedini; Sarajedini et al. 2007), which is a *HST* Treasury project where 66 GCs have been homogeneously observed through the F606W and F814W filters of the Wide Field Camera of the Advanced Camera for Surveys (WFC/ACS). Recently, this dataset has been integrated through the images taken as part of the GO-13227 program (PI: G. Piotto; Piotto et al. 2015), a UV-initiative proposal designed to observe a large sample of clusters through the UV/blue F275W, F336W, and F438W bands of the Ultraviolet and Visual Channel of the Wide Field Camera 3 (UVIS/WFC3) on board *HST*.

Based on multi-band photometry, we estimate the differential reddening associated with each source in the catalog and derive a high-resolution and high-precision reddening map in the directions of 56 Galactic GCs. To do that, we adapt to the available catalogs (Nardiello et al. 2018) the approach by Milone et al. (2012). The main difference is that our dataset comprises magnitudes in five filters, namely F275W, F336W, F438W, F606W, and F814W, whereas the work by Milone and collaborators is based only on the F606W and F814W bands. Our procedure, combining information from five magnitudes, provides more accurate differential-reddening corrections than the previous one. Moreover, we take advantage of stellar proper motions that allow us to separate the bulk of cluster members from field stars in all GCs. The resulting differential-reddening catalogs and the reddening maps are publicly released to the astronomical community.

This paper is organized as follows. Section 2 presents the GC sample and describes the procedures used to identify those stars that provide information on differential reddening. In Section 3 we explain in detail the method to calculate differential reddening, and we estimate the impact of changing the reddening law on the differential-reddening determination. In Section 4 we describe the procedure to constrain the reddening law in the direction of the highly-reddened clusters and we construct high-resolution reddening maps. Finally, Section 5 briefly overviews the results.

2 DATA AND DATA ANALYSIS

To estimate the amount of differential reddening we used the catalogs by Nardiello et al. (2018) that provide astrometric positions, high-precision multi-band photometry, and cluster membership from proper motions in the central $\sim 2.7' \times 2.7'$ FoV for a large sample of 56 Galactic GCs. All the clusters were observed with WFC/ACS camera in F606W and F814W filters as part of the GO-10775 program (PI: A. Sarajedini; Sarajedini et al. 2007) and with UVIS/WFC3 in F275W, F336W, and F438W filters mostly within GO-13227 (PI: G. Piotto; Piotto et al. 2015).

The data reduction has been carried out with the computer program KS2 developed by Jay Anderson as an evolution of *kitchen_sync*, written initially to reduce the images from GO-10775 (Anderson et al. 2008). KS2 derives three distinct astro-photometric catalogs for each cluster obtained through three different methods. Method one provides accurate measurements of bright, unsaturated stars, whereas the photometry of faint stars is best measured with methods two and three (see Sabbi et al. 2016; Bellini et al. 2017; Nardiello et al. 2018; Milone et al. 2022, for details).

In the following, we use photometry from method one. Indeed, the regions of the CMD where the colour broadening is most sensitive

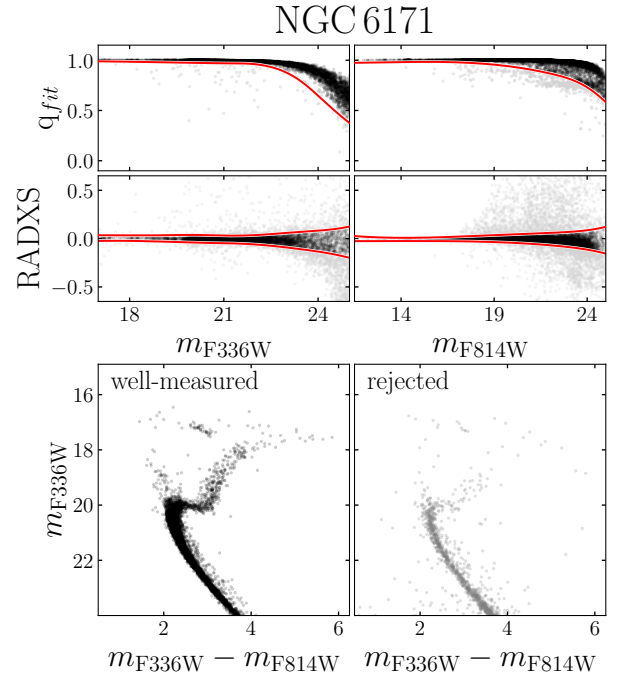


Figure 1. This figure illustrates the procedure to select well-measured stars in NGC 6171. The top and middle panels present the selection based on the q_{fit} (top) and RADXS (middle) parameters. Red lines separate well-measured stars (black points) from those that have poorer photometry (gray points). The m_{F336W} versus $m_{F336W} - m_{F814W}$ CMDs for well-measured stars and for the stars that we rejected are displayed in the bottom-left and the bottom-right panel, respectively.

to differential reddening correspond to the upper MS, SGB, and the lower part of the RGB.

2.1 Selection of well-measured cluster stars

The main impact of differential reddening on the CMD is a colour broadening of the evolutionary sequences. Specifically, the stars that are affected by a larger amount of reddening than the average value exhibit red colours and faint magnitudes relative to the fiducial line derived from all cluster members in the CMD. Conversely, stars with a small amount of reddening are shifted to the bright-blue side of the fiducial.

To estimate the amount of differential reddening associated with each star in the catalog, we need to calculate the shift along the reddening direction relative to the colour and magnitude of a sample of nearby cluster members. However, not all the stars provide information on differential reddening. In the following, we describe the method to identify the probable cluster members with high-quality photometry.

2.1.1 Selection of probable cluster members

The FoVs of GCs are contaminated by a variable number of background/foreground sources. To separate cluster members and field stars, we used the cluster membership probabilities provided by Nardiello et al. (2018, see their Section 4 for details), which corresponds to the probability that a star is part of the cluster based on proper motions. Specifically, we considered probable cluster members all stars with a membership probability greater than 90%.

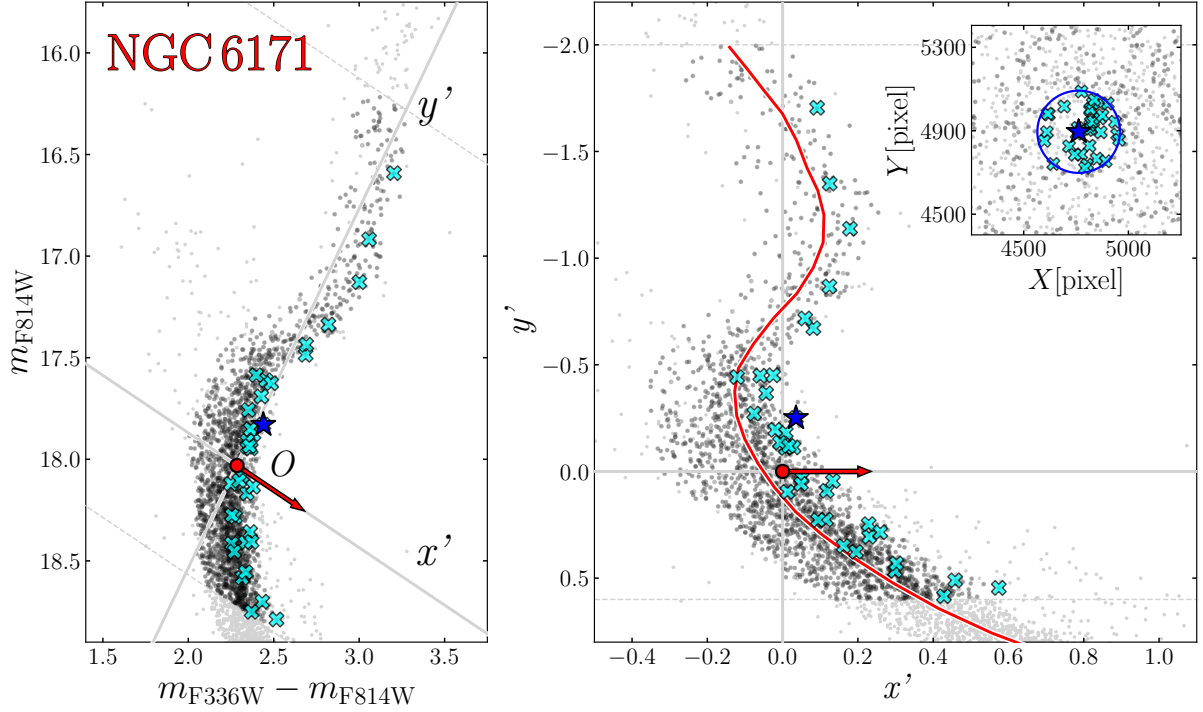


Figure 2. This figure presents the method used to calculate the differential reddening of the target star marked with the large blue starred symbol. In the left panel, we plot the m_{F814W} versus $m_{F336W} - m_{F814W}$ CMD, whereas in the right panel, we show the same stars but in the rotated reference frame. In both diagrams, the red arrow indicates the reddening direction, and black dots, included between the two dotted lines, identify reference stars, among which the 35 closest neighbours of the target star are represented with cyan crosses. The red line is the fiducial of reference stars calculated in the rotated reference frame. Finally, the right-panel inset shows the position of the 35 neighbouring reference stars zoomed around the target star. See Section 3 for details on the employed procedure.

2.1.2 Selection of stars with high-quality photometry

Similarly to differential reddening, photometric uncertainties spread the stars around the fiducial line of the CMD. Hence, it would be challenging to disentangle the effect of reddening and errors from stars with large photometric uncertainties. For this reason, selecting a sample of well-measured stars is mandatory to derive accurate reddening estimates.

For all clusters, our selection criteria rely on the quality fit (q_{fit}) and the RADXS diagnostic parameters, which are provided in the Nardiello et al. (2018) catalogs. Specifically, the q_{fit} estimates the goodness of the PSF-fitting procedure, whereas the RADXS measures the amount of flux that exceeds the predictions from the best-fitting PSF. It is a powerful tool to distinguish cosmic rays and PSF artifacts, which have negative RADXS values, and to identify background galaxies, which have RADXS > 0.

Fig. 1 shows an example of the selection procedure for NGC 6171. In the top and middle panels, we plot the q_{fit} (top) and the RADXS (middle) parameters as a function of magnitudes in the F336W (left) and F814W (right) bands. Red lines are drawn by hand with the criteria for separating well-measured stars (black points) from those that have poorer photometry (gray points). The results of the selection are illustrated in the bottom-left and -right panel, where we show the m_{F336W} versus $m_{F336W} - m_{F814W}$ CMD for well-measured and rejected stars, respectively.

3 DIFFERENTIAL REDDENING DETERMINATION

We dealt with differential reddening by adapting to our dataset the method introduced by Milone et al. (2012) to correct the photometry of 59 Galactic GCs for differential reddening. Our dataset, including magnitudes in the F275W, F336W, F438W, F606W, and F814W bands, allowed us to obtain improved differential-reddening determinations compared to the original ones by Milone et al. (2012), based only on the F606W and F814W magnitudes.

To this aim, we exploited the m_{F814W} versus $m_X - m_{F814W}$ CMDs, where $X = F275W, F336W, F438W,$ and $F606W$, and derived four distinct estimates of the amount of differential reddening suffered by each star. We then averaged together information from the different colour combinations to obtain a more accurate differential-reddening determination. In the following we summarize the adopted procedure, which is illustrated in Fig. 2 for the m_{F814W} versus $m_{F336W} - m_{F814W}$ CMD of NGC 6171 that we used as a test case.

- The reddening vector's direction, which is indicated by the red arrow in the left panel of Fig. 2, has a non-zero slope with respect to CMD axes. To simplify the correction process, we started by defining a new reference frame in which the abscissa (x') and the ordinate (y') are parallel and orthogonal to the reddening direction, respectively. To this aim, we arbitrarily identified a rotation point near the MS turn-off (red dot) and rotated the CMD counterclockwise by an angle θ , defined as:

$$\theta = \arctan \frac{A_{F814W}}{A_X - A_{F814W}} \quad (1)$$

where A_X and A_{F814W} are the absorption coefficients in the X and

F814W filters, respectively (Dotter et al. 2008). A zoom around the SGB of the resulting rotated CMD is presented in the right panel of Fig. 2, where for completeness we also show the rotated direction of the reddening vector (red arrow) and the rotation point. The reddening vector is now parallel to the x' axis.

- We then selected a sample of reference stars in the CMD region that includes the upper MS, the SGB, and the lower portion of the RGB. The reference stars distribute along sequences where there is a wide angular variation between the direction of the fiducial line and that of the reddening vector. Hence, they allow us to disentangle the contribution of photometric errors and differential reddening to the colour broadening. As an example, the selected reference stars of NGC 6171 are marked as black points in the m_{F814W} versus $m_{F336W} - m_{F814W}$ CMD and in the corresponding rotated diagram of Fig. 2.

- We calculated the red fiducial line plotted in the right panel of Fig. 2. To do that, we divided the sample of reference stars into y' bins and we calculated the median values of x' and y' for each of them. We derived the fiducial line of the selected reference stars by linearly interpolating these median points.

- As a final step, we computed the distance from the fiducial line along the reddening direction ($\Delta x'$) by subtracting from the pseudo-colour (x') of each reference star that of the fiducial line at the same y' level.

In summary, this procedure allows us to measure the value of $\Delta x'$ for each reference star. These quantities will be used in Section 3.1, and 4.1 to correct the photometry for the effects of differential reddening and to investigate the reddening in front of the GCs, respectively.

3.1 Correcting the photometry for differential-reddening effects

To derive the amount of differential reddening associated with each star in the catalog, we used an iterative procedure that consists of the following steps:

- For each star in the catalog, we defined a local sample of $N_{\text{ref}} = 30$ -100 nearby reference stars. As an example, in Fig. 2 we mark with cyan crosses the 35 closest reference stars used to estimate the differential reddening suffered by the star represented by the blue starred symbol. As illustrated in the inset of the right panel, all the reference stars lie in a circular region centered on the target star. The radius of this circle, ρ , corresponds to the distance of the farthest reference star with respect to the target one, which is indicative of the map resolution in that specific position. Clearly, the value of ρ changes from one star to another. It is typically small in the central cluster regions, where the density of reference stars is high, and will increase towards the external regions.

- For each star, we calculated the median $\Delta x'$ value of the neighbouring reference-star sample excluding the target from the computation. We estimated the associated error as the root mean scatter of $\Delta x'$ divided by the square root of $N - 1$, where N is the number of selected nearby reference stars. To correct the photometry for the effects of differential reddening we subtracted the derived quantity from the x' value of each star in the rotated reference frame. We then used the new diagram to select reference stars with more accuracy and therefore obtain an improved fiducial line.

- We repeated all steps above until the procedure converges. Typically, this happens after three iterations. At this point, we converted the corrected x' and y' into m_X and m_{F814W} magnitudes and we used the corresponding absorption coefficients to derive the differential-reddening value associated with each star.

The best differential-reddening estimate for each star is obtained

by combining the information from the different m_{F814W} versus $m_X - m_{F814W}$ CMDs. Specifically, our final estimate of ΔA_{F814W} corresponds to the weighted average of the four distinct differential-reddening determinations. The corresponding uncertainties are given by the error of the weighted mean.

We derived various determinations of differential reddening by assuming different values of N_{ref} ranging from 30 to 100 in step of 5. For each differential-reddening determination, we calculated the residuals between the corrected x' values and the fiducial line in each CMD. The best determination of differential reddening is provided by the value of N_{ref} that gives the minimum values of the r.m.s of these residuals.

As an example, the results of this procedure are illustrated in panels a and b of Fig. 3 for NGC 6171, where we compare the original m_{F814W} versus $m_{F336W} - m_{F814W}$ CMD and the corresponding diagram corrected for differential reddening. Noticeably, the evolutionary sequences in the corrected CMD are consistently narrower than in the original one. In panel c of Fig. 3 we provide the resulting high-resolution differential-reddening map, whereas in panel d we show the variation of the resolution in the observed FoV of the cluster. As expected, the highest resolution ($\rho = 5.5$ arcsec) is achieved in the central regions of the cluster where the density of the reference stars is higher.

For 21 out of 56 GCs, the photometry corrected for differential reddening provides improved CMDs, thus demonstrating the efficiency of the correction. Conversely, the correction for differential reddening does not improve the photometry of the remaining 35 GCs. This fact is not surprising. Indeed these clusters have $E(B - V) \lesssim 0.01$ mag and the amount of differential reddening is likely comparable to or smaller than the uncertainties of $E(B - V)$ determinations.

In Table 1 we provide for each cluster the minimum, maximum, and median value of ρ used to derive the differential reddening of cluster members (ρ_{min} , ρ_{max} , and ρ_{med}). The average values of ρ_{min} , ρ_{max} , and ρ_{med} for all clusters are 5.6, 41.9, and 11.6 arcsec, respectively.

3.2 The impact of the reddening law on differential-reddening determination

The interstellar reddening law, namely the relation between the absorption coefficient A_λ and the wavelength, has been expressed in several ways by different authors in the literature (e.g., Cardelli et al. 1989; Fitzpatrick & Massa 1990; O'Donnell 1994). All of these formulations depend on a single parameter, $R_V = A_V / E(B - V)$, which is usually set to 3.1, the standard value for the diffuse interstellar medium (e.g., Sneden et al. 1978). However, it is well known that the extinction law is not uniform in the Galaxy, and the value of R_V changes from place to place. For example, several authors found that $R_V \sim 2.5$ is an appropriate value to describe the reddening law toward the Galactic Center (e.g., Udalski 2003; Nataf et al. 2013, 2016). In addition, R_V can change significantly also in nearby regions, as in the case of the ρ Ophiuchi cloud, where $R_V = 4.1$ (Cardelli et al. 1989; Hendricks et al. 2012). Similarly, the investigation of the various regions of recent star formation in the Large Magellanic Cloud revealed that the extinction curve is systematically flatter (in logarithmic units) than in the diffuse interstellar medium (De Marchi & Panagia 2014, 2019; De Marchi et al. 2016, 2020, 2021).

In the upper panel of Fig. 4 we show three curves corresponding to the extinction laws derived assuming the O'Donnell (1994) parametrization and three different values of R_V , namely 2.5 (red), 3.1 (gray), and 4.1 (blue). The bottom panel of Fig. 4 illustrates the

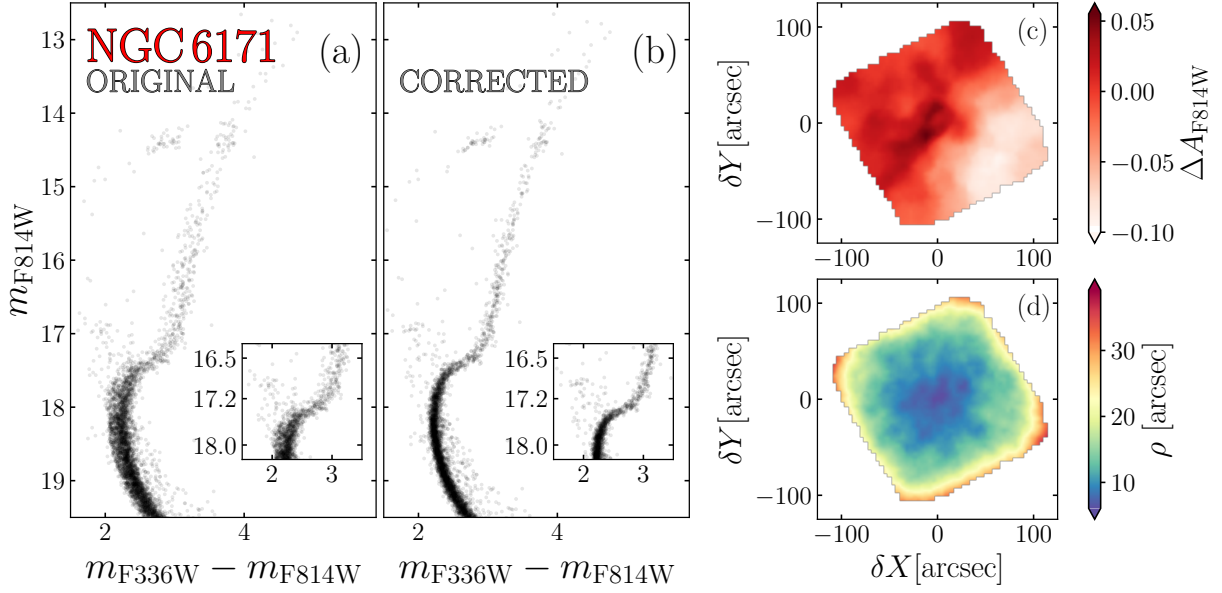


Figure 3. Panel a-b. Comparison between the original m_{F814W} versus $m_{F336W} - m_{F814W}$ CMD of NGC 6171 and the corresponding photometric diagram corrected for differential reddening. In the inset, we plotted a zoom around the SGB where the correction is more evident. Panel c. Differential-reddening map in the direction of NGC 6171. The levels of red are proportional to the reddening variation as indicated by the associated colour bar on the right. Panel d. Variation of the resolution of the differential-reddening correction within the observed FoV.

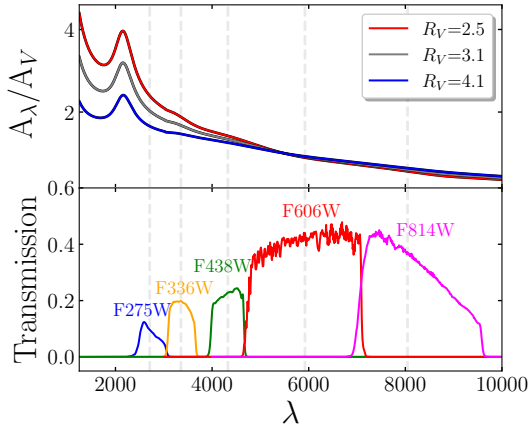


Figure 4. Upper panel. Extinction law for three different assumptions of the R_V coefficient, namely the standard value for diffuse interstellar medium (3.1, gray line), the value commonly assumed in the direction of the Galactic Center (2.5, red line) and the value measured for the ρ Ophiuchi cloud (4.1, blue line). The vertical dashed lines are drawn corresponding to the central wavelengths of the five photometric filters used in this work. Bottom panel. Transmission curves of the five filters used in this work to correct photometry for differential reddening.

transmission curves of the five filters used in this work to estimate differential reddening.

To verify whether different values of R_V can significantly alter the outcomes of the procedure to correct photometry, we corrected the CMDs of NGC 6171 with the same procedure described in Section 3 by assuming a non-universal reddening law. Specifically, we calculated differential reddening in the case of $R_V = 2.5$ and $R_V = 4.1$, and then we compared the results with our previous determination, derived assuming $R_V = 3.1$. To do that, we first determined the absorption coefficients in the UVIS/WFC3 F275W, F336W, and F438W

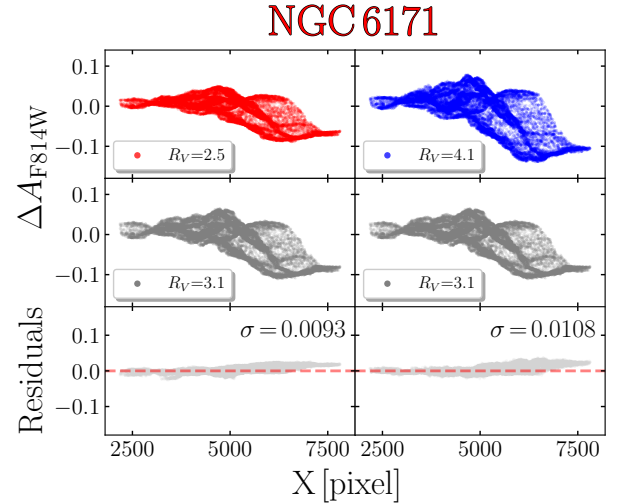


Figure 5. Local reddening variations in the direction of NGC 6171 as a function of the X coordinates calculated by assuming $R_V = 2.5$ (upper-left panel), $R_V = 4.1$ (upper-right panel), and $R_V = 3.1$ (middle panels). Bottom panels illustrate the residuals, derived by comparing ΔA_{F814W} calculated by assuming $R_V = 2.5$ (left) and $R_V = 4.1$ (right), respectively, with the original ΔA_{F814W} , obtained by assuming $R_V = 3.1$. The dashed red line marks the average difference, whereas the dispersion of the residuals is reported in the upper-right corner.

filters and in the WFC/ACS F606W and F814W bands. We used a synthetic spectrum of a star with effective temperature $T_{\text{eff}} = 5900$ K, gravity $\log g = 4.5$, and metallicity $[\text{Fe}/\text{H}] = -1.5$ as reference. Then, we derived an absorbed spectrum by convolving the flux of the reference spectrum with the extinction law by O'Donnell (1994). To this aim, we assumed $E(B - V) = 0.33$ (from the 2010 version of Harris 1996, catalog) and $R_V = 2.5$ and 4.1, respectively. The two

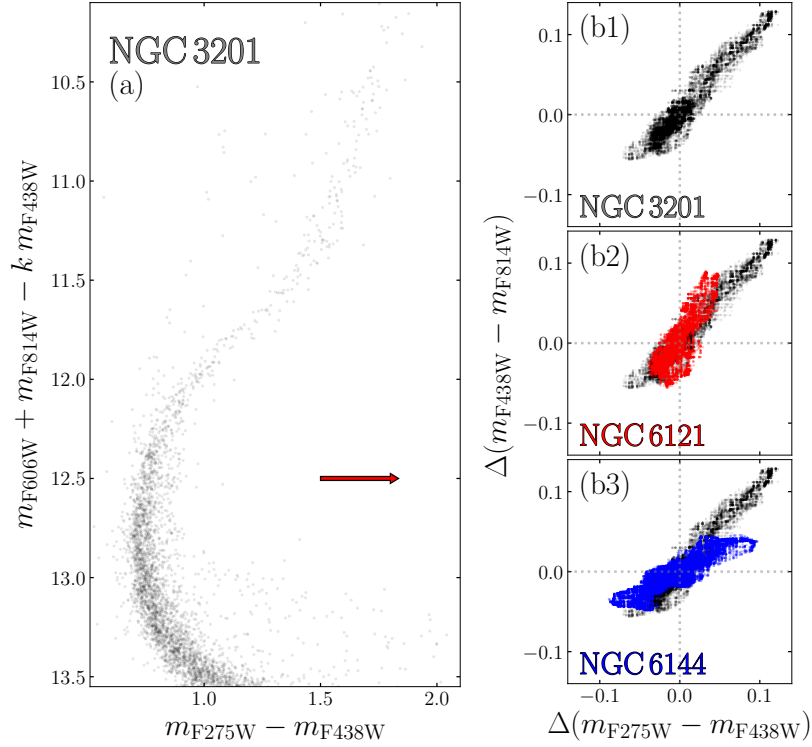


Figure 6. $m_{F606W} + m_{F814W} - k m_{F438W}$ versus $m_{F275W} - m_{F438W}$ pseudo-CMD of NGC 3201 (panel a). $\Delta(m_{F438W} - m_{F814W})$ versus $\Delta(m_{F275W} - m_{F438W})$ diagrams for NGC 3201 (b1), NGC 6121 (b2), and NGC 6144 (b3).

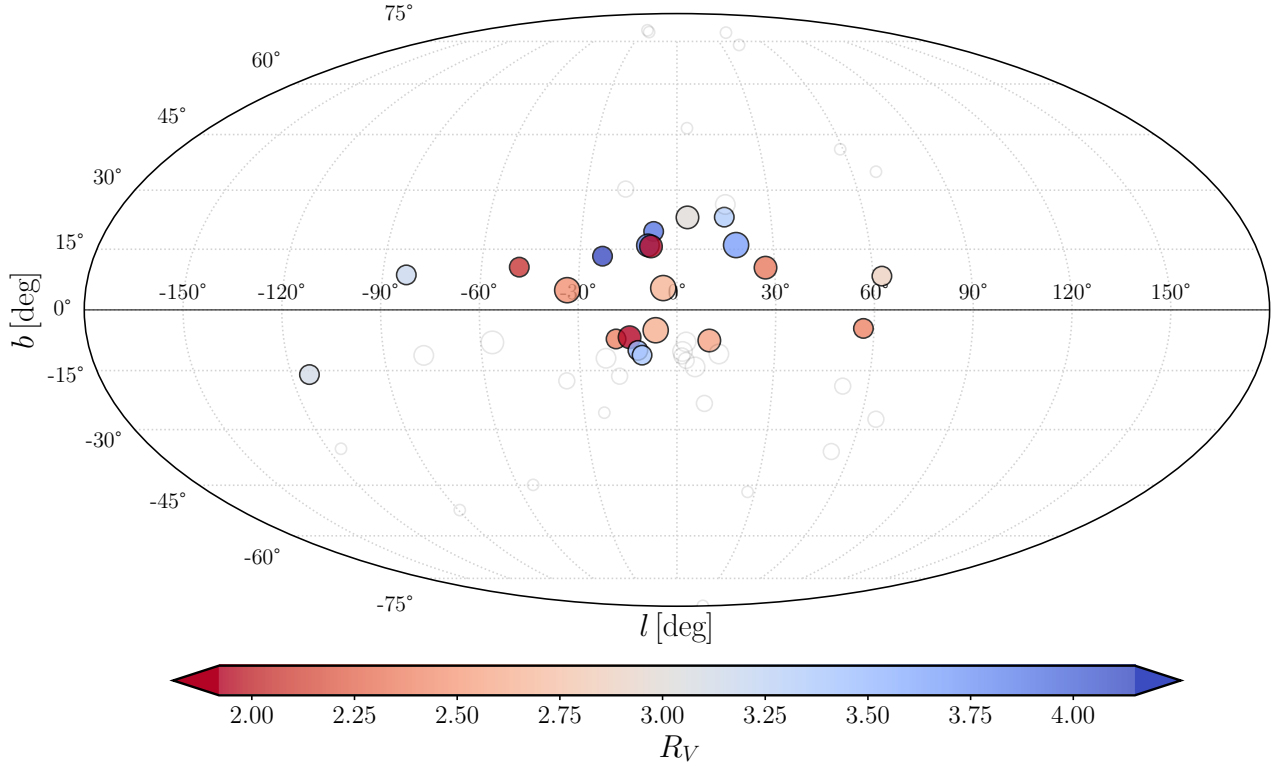


Figure 7. Spatial distribution of the 56 GCs studied in this work in Galactic coordinates. The size of each point is proportional to the average reddening of the cluster. The 21 GCs for which the corrected photometry provides improved CMDs are colour-coded according to the measured R_V in their FoV.

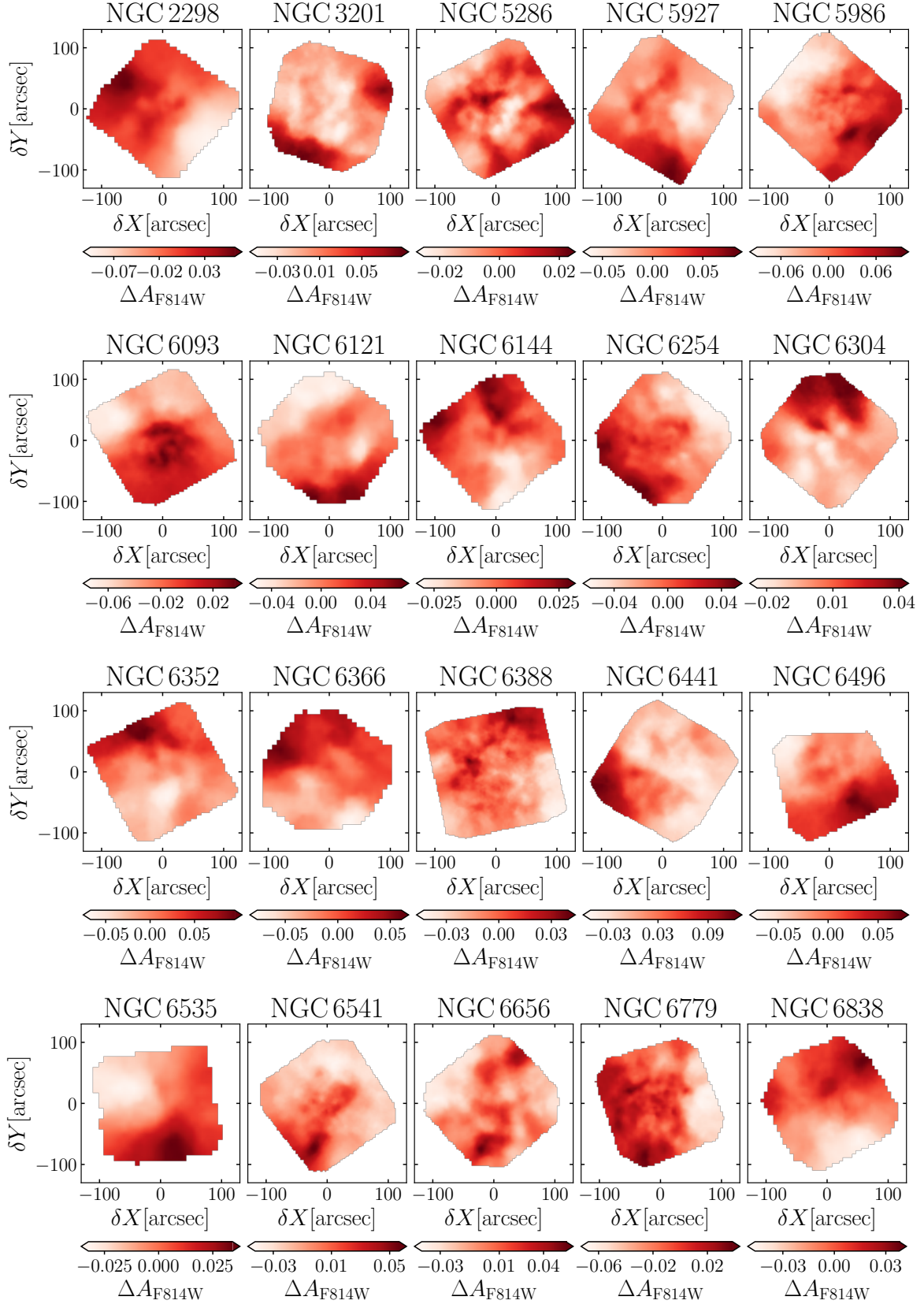


Figure 8. Differential-reddening maps in the direction of twenty Galactic GCs. The colour bar in the bottom panel of each plot codifies the ΔA_{F814W} values ranging from less extinct regions (lighter colours) to more extinct areas (redder colours).

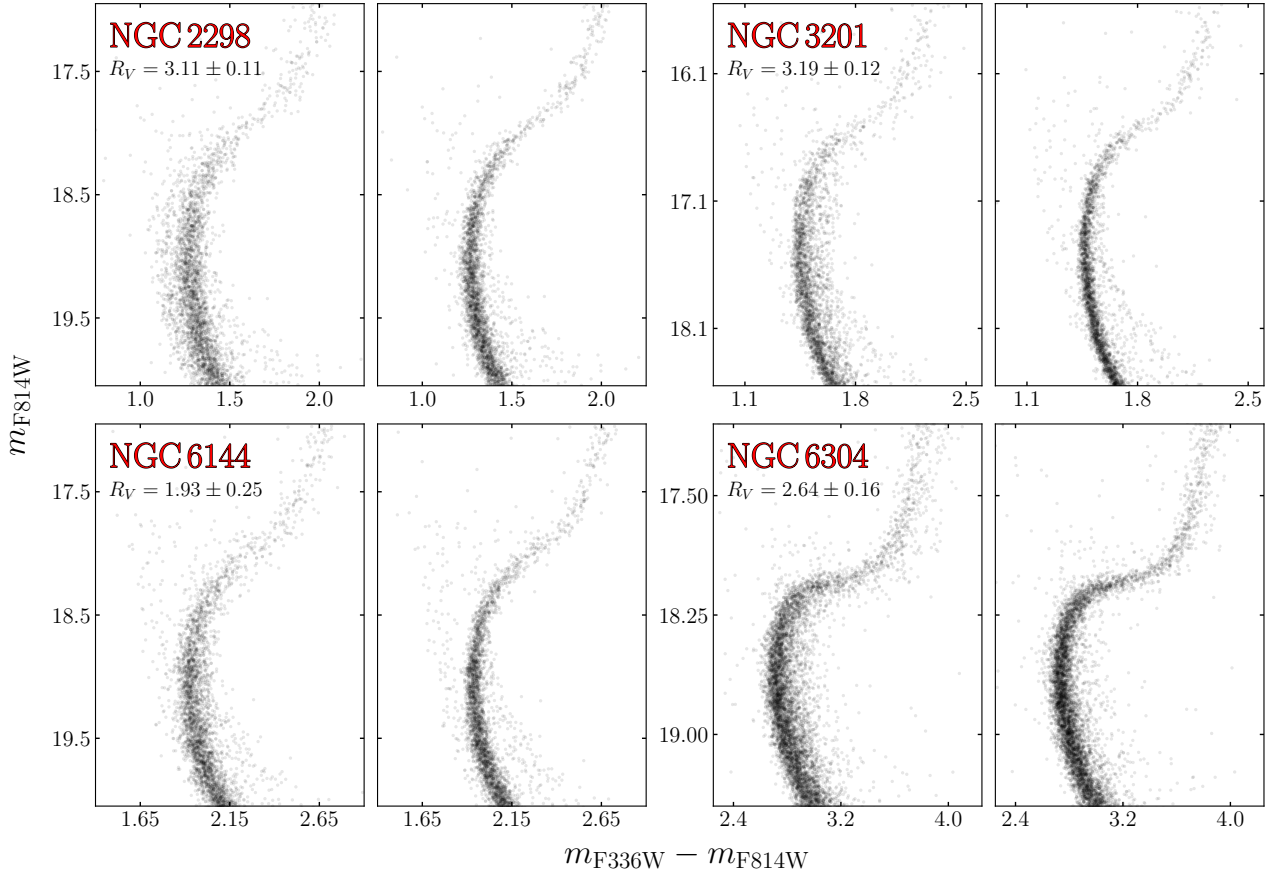


Figure 9. m_{F814W} versus $m_{F336W} - m_{F814W}$ CMDs for four GCs before (left panel) and after (right panel) applying the procedure to correct for differential reddening.

synthetic spectra have been integrated over the transmission curves of the filters used in this paper to derive the corresponding magnitudes. Finally, by comparing the magnitudes of the absorbed and the reference spectrum we found the absorption coefficients that we used to derive the direction of the reddening vector.

Results are illustrated in Fig. 5, where we show the local reddening variations as a function of the X coordinate derived assuming $R_V = 2.5$, $R_V = 4.1$, and $R_V = 3.1$. The bottom panels show the residuals calculated comparing ΔA_{F814W} derived assuming $R_V = 2.5$ (left) and $R_V = 4.1$ (right), with the original ΔA_{F814W} distribution, derived assuming $R_V = 3.1$. In both cases, we obtained an average difference close to zero and a dispersion, $\sigma \sim 0.01$ mag. We found similar results for NGC 6441, which is the GC that shows the highest variations of reddening in the FoV.

We conclude that changing R_V has a moderate impact on the differential-reddening map of highly-reddened clusters. The effect is negligible for the GCs that exhibit small reddening variations in their FoV, which include most of the investigated objects. In the following Section, we constrain the reddening law in the direction of the 21 GCs that are significantly affected by differential reddening and improve their differential-reddening map.

4 THE REDDENING LAW IN THE DIRECTION OF 21 CLUSTERS

For 21 out of 56 GCs, the photometry corrected for differential reddening provides improved CMDs. These clusters, which are significantly affected by differential reddening, offer us the possibility to constrain the reddening law within the Galaxy in their directions.

To do that we adopted the following iterative procedure. We first constructed the $m_{F606W} + m_{F814W} - km_{F438W}$ versus $m_{F275W} - m_{F438W}$ and $m_{F606W} + m_{F814W} - km_{F438W}$ versus $m_{F438W} - m_{F814W}$ pseudo-CMDs. The constant k is chosen in such a way that the combination of magnitudes in the y-axis is reddening-free so that the differential reddening affects only the colour on the x-axis. Similar to the values of absorption in the F438W, F606W, and F814W bands, k depends on the reddening law. At the first iteration, we assumed the O'Donnell (1994) reddening law with $R_V = 3.1$, which corresponds to $k = 1.19$. As an example, we show the $m_{F606W} + m_{F814W} - km_{F438W}$ versus $m_{F275W} - m_{F438W}$ diagram of NGC 3201 in panel a of Fig. 6, where we use a red arrow to indicate the reddening direction.

We used each pseudo-CMD to derive the amount of reddening that affects the $m_{F275W} - m_{F438W}$ and $m_{F438W} - m_{F814W}$ of each star ($\Delta(m_{F275W} - m_{F438W})$ and $\Delta(m_{F438W} - m_{F814W})$) by using the procedure of Section 3.

To constrain the value of R_V in the direction of the investigated targets we compared the slopes of the observed points in the $\Delta(m_{F438W} - m_{F814W})$ versus $\Delta(m_{F275W} - m_{F438W})$ diagram

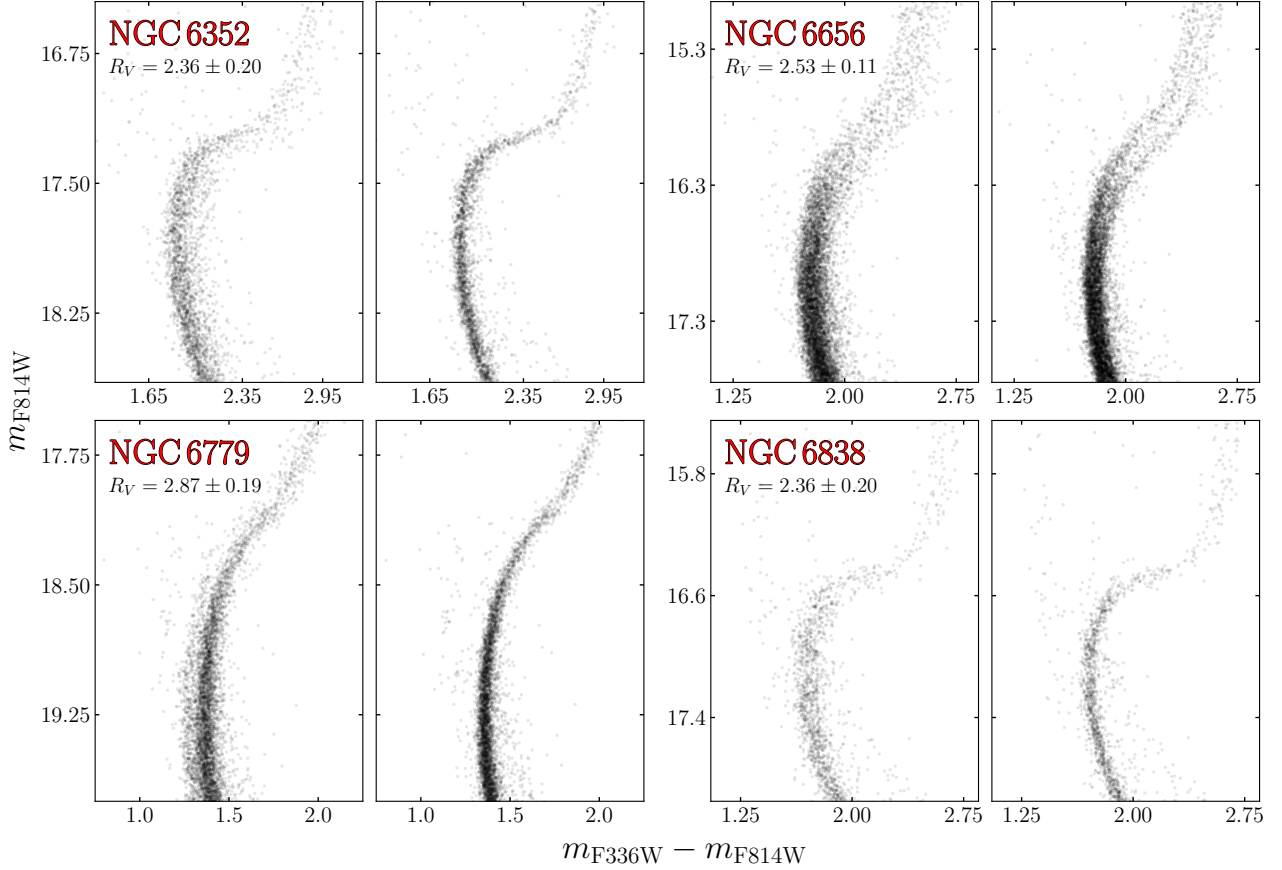


Figure 10. Same as in Fig. 9 but for NGC 6352, NGC 6656, NGC 6779, and NGC 6838.

with the values inferred from simulated photometry. The latter comprises the same number of stars, observational errors, and $\Delta(m_{F438W} - m_{F814W})$ distribution as derived from the observed CMD. We assumed the O'Donnell (1994) reddening law and various values of R_V ranging from 1.5 to 5.0 in steps of 0.1. For each value of R_V , we calculated the slope of the least-squares best-fit line in the $\Delta(m_{F438W} - m_{F814W})$ versus $\Delta(m_{F275W} - m_{F438W})$ plane. The value of R_V that provides the smallest difference between the slopes of the line derived from simulated and observed points corresponds to the best determination of R_V . This ends one iteration. At this stage, we repeated the procedure above by using the updated value of R_V .

The results for NGC 3201 ($R_V = 3.19 \pm 0.12$) are illustrated in the panel b1, whereas panels b2 and b3 compare the results obtained in the directions of NGC 6121 (red, $R_V = 3.85 \pm 0.13$) and NGC 6144 (blue, $R_V = 1.93 \pm 0.25$) with NGC 3201. Clearly, the distributions of points in the $\Delta(m_{F438W} - m_{F814W})$ versus $\Delta(m_{F275W} - m_{F438W})$ plane are consistent with lines that have different slopes.

The resulting values of R_V are listed in Table 2 and range from ~ 2.0 to ~ 4.0 with a high level of variability within the Galaxy. In Fig. 7 we plot the spatial distribution of the studied GCs in Galactic coordinates, colour-coded according to the measured values of R_V . Typically, the clusters that are close to the Galactic plane and in proximity to the Galactic center exhibit smaller values of R_V than the standard one.

We used the updated values of R_V to calculate the direction of the reddening vector and then provide a more precise determination of local reddening variations in the direction of the 21 highly-reddened

targets within our sample. The reddening maps in the direction of these clusters are provided in Fig. 8 (the map for NGC 6171 is already shown in panel c of Fig. 3), whereas in Fig. 9 and 10 we show the original (left panels) and corrected (right panels) m_{F814W} versus $m_{F336W} - m_{F814W}$ CMDs for eight GCs. These plots point out the effectiveness of the adopted method, as in all presented GCs the CMD region including the upper MS, the SGB, and the lower part of the RGB appears sharper and better defined.

For each of the 21 clusters, we publicly release the photometry of all stars in the catalogs corrected for differential reddening, together with the corresponding high-resolution reddening map. Specifically, for each star, we provide the ID (from Nardiello et al. 2018), the amount of differential reddening with the corresponding uncertainty, and the value of ρ .

4.1 Reddening in the directions of 56 Globular Clusters

The procedure presented in Section 3.1 provides high-precision differential reddening estimates that allowed us to significantly improve the photometry of 21 GCs. However, the radii of the regions used to derive the amount of differential reddening associated with each star change from one star to another, thus making it challenging to compare the results from the different clusters.

To further quantify the amount of differential reddening and better compare the reddening variation in the direction of each cluster, we divided the FoV into a regular grid of $\sim 7 \times 7$ arcsec² cells. We calculated the median $\Delta x'$ of reference stars inside each cell and converted this quantity into the corresponding differential-reddening value us-

ing the absorption coefficients. We estimated the uncertainty as the ratio between the dispersion of the differential-reddening values of the stars in each cell divided by the square root on $N - 1$, where N is the number of stars in that cell. We then derived the weighted average of the four distinct estimates of ΔA_{F814W} obtained from the m_{F814W} versus $m_X - m_{F814W}$ CMDs, where $X=F275W, F336W, F438W$, and $F606W$.

Table 1 provides $\sigma_{\Delta A_{F814W}}$ and $\Delta A_{F814W,max}$, respectively the 68.27th percentile and the difference between the 98th and the 2nd percentile of the differential-reddening distribution. We estimated the corresponding errors by means of bootstrapping statistics. Specifically, we generated 1,000 samples and for each extraction, we used the method presented above to obtain an estimate of $\sigma_{\Delta A_{F814W}}$ and $\Delta A_{F814W,max}$. The uncertainties associated with these two quantities correspond to the random mean scatter of the 1,000 determinations.

Since the FoVs of all studied clusters span a similar area, the results from our analysis allow us to compare the reddening along the directions of the 56 GCs. We used $\sigma_{\Delta A_{F814W}}$ and $\Delta A_{F814W,max}$ to quantify the variation of extinction across the observed FoV. Specifically, we assumed $\sigma_{\Delta A_{F814W}}$ and $\Delta A_{F814W,max}$ as a proxy of the average and maximum differential-reddening variation, respectively.

The values of $\sigma_{\Delta A_{F814W}}$ range from 0.003 mag to 0.030 mag, whereas $\Delta A_{F814W,max}$ varies from a minimum of 0.012 mag to a maximum of 0.120 mag. As shown in Fig. 11, where we plot the spatial distribution of the studied GCs in Galactic coordinates (l,b), the GCs with large values of $\sigma_{\Delta A_{F814W}}$ are located in the proximity of the Galactic plane. Specifically, $\sigma_{\Delta A_{F814W}}$ exhibits a significant anti-correlation with the absolute value of the Galactic latitude (left panel of Fig. 12), and a strong correlation with the average reddening of the host cluster (from the 2010 version of the Harris 1996, catalog, right panel of Fig. 12).

Our results corroborate previous findings that highly-reddened GCs typically show higher differential-reddening variations across their FoV (Bonatto et al. 2013; Jang et al. 2022). However, we note large variations of the $\sigma_{\Delta A_{F814W}}$ value among clusters with similar reddening. A remarkable example is provided by the two clusters with the highest $E(B - V)$ values, NGC 6366 and NGC 6304, which are characterized by low values of $\sigma_{\Delta A_{F814W}}$ with respect to the common trend. These facts would suggest that in addition to $E(B - V)$, another parameter is responsible for the value of $\sigma_{\Delta A_{F814W}}$. Similar conclusions can be extended to $\Delta A_{F814W,max}$.

5 SUMMARY AND CONCLUSIONS

Our group has undertaken an extensive investigation of differential reddening in the directions of the Galactic and Magellanic Cloud star clusters based on multi-band photometry from *HST* and wide-field ground-based telescopes (Jang et al. 2022; Milone et al. 2022). In the present work, we estimated the amount of differential reddening in the direction of 56 Galactic GCs based on *HST* photometry. To do that, we adapted the method by Milone et al. (2012) to archival data uniformly observed through the F275W, F336W, F438W of UVIS/WFC3, and the F606W, and F814W filters of WFC/ACS (Nardiello et al. 2018). We derived the amount of differential reddening associated with all stars in the catalogs with a typical spatial resolution of ~ 12 arcsec.

We used these differential-reddening values to correct photometry for the effects of absorption. For 21 out of 56 GCs with reddening variations $\sigma_{\Delta A_{F814W}} \gtrsim 0.01$ we obtain improved CMDs, as all evolutionary sequences become thinner and better defined. In addition, we constrained the reddening law in the direction of these clusters. To do that, we compared the slopes of the observed points

in the $\Delta(m_{F275W} - m_{F438W})$ versus $\Delta(m_{F438W} - m_{F814W})$ diagram with the values inferred from simulated photometry derived assuming various values of R_V . We found that R_V exhibits a high level of variability within the Galaxy, with values ranging from ~ 2.0 to ~ 4.0 . The updated values of R_V have been used to calculate the direction of the reddening vector and then derive a more precise determination of local reddening variations within the FoV of the 21 highly-reddened targets. For these clusters, we publicly release the photometric catalogs corrected for differential reddening, together with the corresponding reddening map.

To quantify the variation of reddening across the observed FoV and compare the results from the different clusters, we computed the 68.27th percentile ($\sigma_{\Delta A_{F814W}}$) and the difference between the 98th and the 2nd percentile ($\Delta A_{F814W,max}$) of the differential-reddening distribution. We found that $\sigma_{\Delta A_{F814W}}$ ranges from 0.003 to 0.030 mag, whereas $\Delta A_{F814W,max}$ varies from 0.012 to 0.120 mag. The 68.27th percentile of the differential-reddening distribution exhibits a strong correlation with the average reddening of the host cluster. In addition, GCs with large values of $\sigma_{\Delta A_{F814W}}$ are located in the proximity of the Galactic plane, as we found that there is a significant anti-correlation between $\sigma_{\Delta A_{F814W}}$ and the absolute module of the Galactic latitude. Similar results have been found for $\Delta A_{F814W,max}$, thus corroborating the conclusion that GCs with high values of average reddening are affected by large amounts of differential reddening.

ACKNOWLEDGEMENTS

We thank the anonymous referee for various suggestions that improved the quality of the manuscript. This work has received support from the European Research Council (ERC) under the European Union's Horizon 2020 research innovation programme (Grant Agreement ERC-StG 2016, No 716082 'GALFOR', PI: Milone, <http://progetti.dfa.unipd.it/GALFOR>). APM and ED acknowledge support from MIUR through the FARE project R164RM93XW SEMPLICE (PI: Milone) and from MIUR under PRIN program 2017Z2HSMF (PI: Bedin).

DATA AVAILABILITY

The data underlying this article will be shared on reasonable request to the corresponding author.

REFERENCES

- Anderson J., et al., 2008, *AJ*, **135**, 2055
- Bellini A., Anderson J., Bedin L. R., King I. R., van der Marel R. P., Piotto G., Cool A., 2017, *ApJ*, **842**, 6
- Bonatto C., Campos F., Kepler S. O., 2013, *MNRAS*, **435**, 263
- Cardelli J. A., Clayton G. C., Mathis J. S., 1989, *ApJ*, **345**, 245
- Cordoni G., Milone A. P., Mastrobuono-Battisti A., Marino A. F., Lagioia E. P., Tailo M., Baumgardt H., Hilker M., 2020, *ApJ*, **889**, 18
- De Marchi G., Panagia N., 2014, *MNRAS*, **445**, 93
- De Marchi G., Panagia N., 2019, *ApJ*, **878**, 31
- De Marchi G., et al., 2016, *MNRAS*, **455**, 4373
- De Marchi G., Panagia N., Milone A. P., 2020, *ApJ*, **899**, 114
- De Marchi G., Panagia N., Milone A. P., 2021, *ApJ*, **922**, 135
- Dondoglio E., Milone A. P., Lagioia E. P., Marino A. F., Tailo M., Cordoni G., Jang S., Carlos M., 2021, *ApJ*, **906**, 76
- Dondoglio E., et al., 2022, *ApJ*, **927**, 207
- Dotter A., Chaboyer B., Jevremović D., Kostov V., Baron E., Ferguson J. W., 2008, *ApJS*, **178**, 89

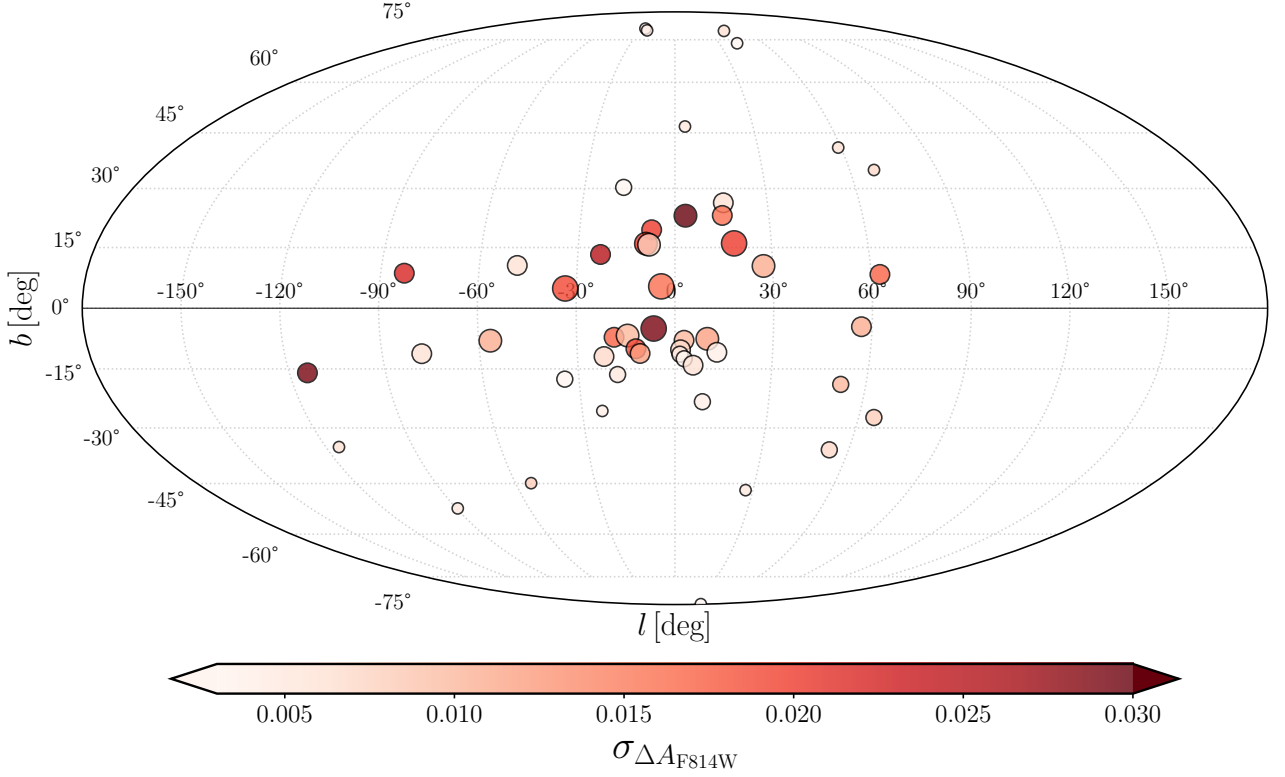


Figure 11. Spatial distribution of the 56 GCs studied in this work in Galactic coordinates. The size of each point is proportional to the average reddening of the cluster, whereas the levels of red are indicative of the 68th percentile of the differential-reddening variation, as indicated by the colour bar on the bottom.

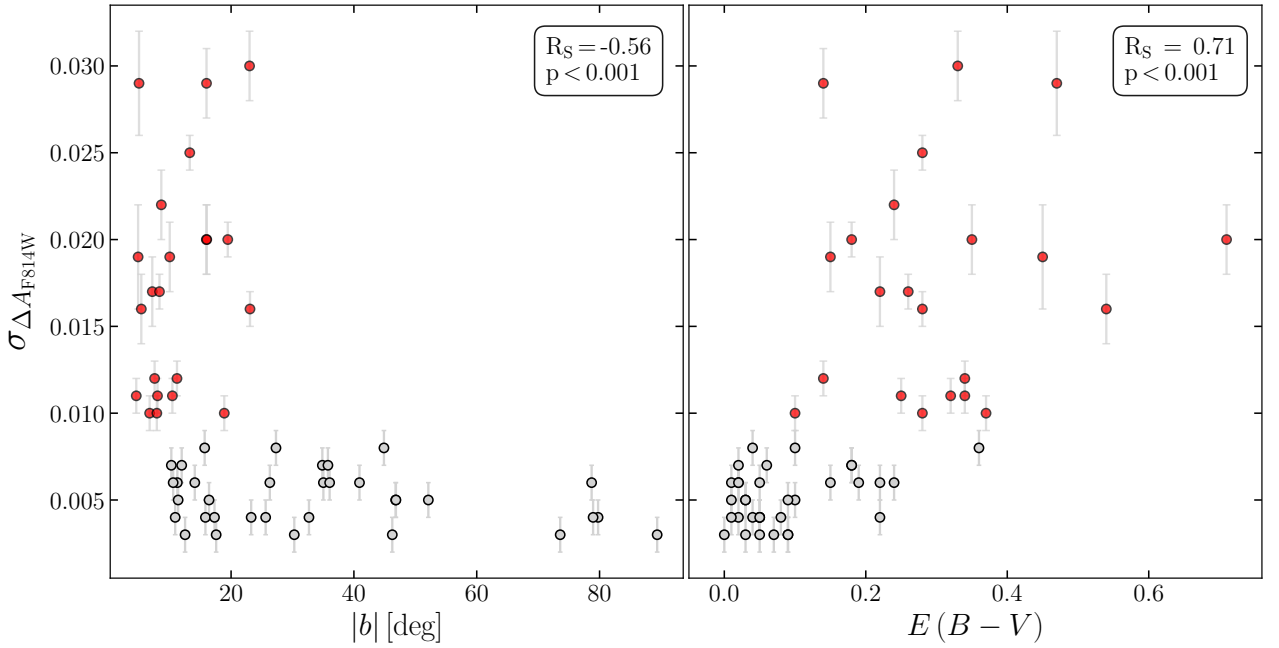


Figure 12. *Left panel.* 68th percentile of the differential-reddening variation, $\sigma_{\Delta A_{F814W}}$, against the absolute value of the Galactic latitude. *Right panel.* $\sigma_{\Delta A_{F814W}}$ as a function of the average reddening calculated in the direction of the cluster. Red dots represent the 21 GCs for which the photometry corrected for differential reddening provides improved CMDs. The Spearman's rank correlation coefficient and the associated p-value are quoted in the upper-right corner.

Table 1. This table lists for each cluster the average reddening (from the 2010 version of the [Harris 1996](#), catalog), the 68th percentile of the differential-reddening distribution, the maximum variation of differential reddening across the FoV of the cluster (difference between the 98th and the 2nd percentile of the differential-reddening distribution), the minimum, maximum, and median radius of the regions used to estimate differential reddening in the observed FoV.

Cluster ID	$E(B - V)$ (mag)	$\sigma_{\Delta A_{F814W}}$ (mag)	$\Delta A_{F814W, max}$ (mag)	ρ_{min} (arcsec)	ρ_{max} (arcsec)	ρ_{med} (arcsec)
NGC 0104	0.04	0.008 ± 0.001	0.031 ± 0.004	4.1	66.2	8.4
NGC 0288	0.03	0.003 ± 0.001	0.012 ± 0.003	9.1	39.1	13.6
NGC 0362	0.05	0.003 ± 0.001	0.013 ± 0.001	4.1	48.9	6.9
NGC 1261	0.01	0.005 ± 0.001	0.016 ± 0.002	3.8	40.1	9.0
NGC 1851	0.02	0.006 ± 0.001	0.022 ± 0.002	3.8	32.9	7.2
NGC 2298	0.14	0.029 ± 0.002	0.098 ± 0.008	5.2	57.6	16.2
NGC 2808	0.22	0.006 ± 0.001	0.021 ± 0.001	5.5	23.8	8.0
NGC 3201	0.24	0.022 ± 0.002	0.078 ± 0.005	6.6	32.2	12.7
NGC 4590	0.05	0.006 ± 0.001	0.020 ± 0.002	4.1	38.6	10.6
NGC 4833	0.32	0.011 ± 0.001	0.044 ± 0.006	4.3	21.0	8.1
NGC 5024	0.02	0.004 ± 0.001	0.014 ± 0.002	4.8	35.7	8.2
NGC 5053	0.01	0.004 ± 0.001	0.015 ± 0.002	12.9	50.3	20.2
NGC 5272	0.01	0.006 ± 0.001	0.020 ± 0.001	4.8	56.6	8.0
NGC 5286	0.24	0.006 ± 0.001	0.022 ± 0.004	5.2	40.5	9.5
NGC 5466	0.00	0.003 ± 0.001	0.013 ± 0.002	9.8	39.1	15.3
NGC 5897	0.09	0.003 ± 0.001	0.012 ± 0.001	7.5	30.4	12.2
NGC 5904	0.03	0.005 ± 0.001	0.016 ± 0.001	4.0	71.4	9.0
NGC 5927	0.45	0.019 ± 0.003	0.076 ± 0.012	5.7	43.3	12.5
NGC 5986	0.28	0.025 ± 0.001	0.086 ± 0.004	3.9	37.1	8.0
NGC 6093	0.18	0.020 ± 0.001	0.066 ± 0.005	5.4	52.1	10.1
NGC 6101	0.05	0.004 ± 0.001	0.014 ± 0.001	5.7	36.4	11.5
NGC 6121	0.35	0.020 ± 0.002	0.082 ± 0.012	11.3	43.1	19.8
NGC 6144	0.36	0.008 ± 0.001	0.028 ± 0.002	6.4	32.7	11.7
NGC 6171	0.33	0.030 ± 0.002	0.100 ± 0.004	5.5	39.2	11.9
NGC 6205	0.02	0.006 ± 0.001	0.021 ± 0.001	4.3	35.8	7.5
NGC 6218	0.19	0.006 ± 0.001	0.022 ± 0.001	6.6	28.8	12.1
NGC 6254	0.28	0.016 ± 0.001	0.052 ± 0.003	4.1	27.2	8.7
NGC 6304	0.54	0.016 ± 0.002	0.061 ± 0.007	5.5	47.7	18.3
NGC 6341	0.02	0.007 ± 0.001	0.022 ± 0.001	4.2	30.5	8.5
NGC 6352	0.22	0.017 ± 0.002	0.070 ± 0.010	7.3	40.2	14.4
NGC 6362	0.09	0.003 ± 0.001	0.013 ± 0.001	7.3	36.3	12.3
NGC 6366	0.71	0.020 ± 0.002	0.078 ± 0.006	12.4	46.0	20.8
NGC 6388	0.37	0.010 ± 0.001	0.038 ± 0.005	5.5	39.4	8.1
NGC 6397	0.18	0.007 ± 0.001	0.025 ± 0.003	3.1	40.6	13.2
NGC 6441	0.47	0.029 ± 0.003	0.120 ± 0.013	6.2	39.6	9.1
NGC 6496	0.15	0.019 ± 0.002	0.072 ± 0.007	5.6	43.6	13.0
NGC 6535	0.34	0.011 ± 0.001	0.043 ± 0.006	6.6	81.9	25.9
NGC 6541	0.14	0.012 ± 0.001	0.048 ± 0.006	4.5	34.9	10.4
NGC 6584	0.10	0.005 ± 0.001	0.019 ± 0.002	3.1	41.2	8.1
NGC 6624	0.28	0.010 ± 0.001	0.042 ± 0.008	3.8	43.5	11.7
NGC 6637	0.18	0.007 ± 0.001	0.025 ± 0.002	2.8	34.7	7.3
NGC 6652	0.09	0.005 ± 0.001	0.020 ± 0.003	3.0	50.8	12.9
NGC 6656	0.34	0.012 ± 0.001	0.047 ± 0.002	7.3	30.9	12.4
NGC 6681	0.07	0.003 ± 0.001	0.013 ± 0.001	2.9	37.4	9.9
NGC 6715	0.15	0.006 ± 0.001	0.022 ± 0.002	6.2	70.0	11.2
NGC 6717	0.22	0.004 ± 0.001	0.017 ± 0.003	4.6	54.4	23.3
NGC 6723	0.05	0.004 ± 0.001	0.017 ± 0.002	3.4	24.2	7.2
NGC 6752	0.04	0.004 ± 0.001	0.015 ± 0.002	2.6	85.7	10.0
NGC 6779	0.26	0.017 ± 0.001	0.057 ± 0.003	2.9	29.4	7.6
NGC 6809	0.08	0.004 ± 0.001	0.014 ± 0.001	8.6	31.9	14.0
NGC 6838	0.25	0.011 ± 0.001	0.039 ± 0.002	11.9	44.6	19.2
NGC 6934	0.10	0.010 ± 0.001	0.034 ± 0.005	4.1	44.5	9.4
NGC 6981	0.05	0.004 ± 0.001	0.015 ± 0.001	3.6	42.1	9.5
NGC 7078	0.10	0.008 ± 0.001	0.029 ± 0.002	5.2	33.3	8.3
NGC 7089	0.06	0.007 ± 0.001	0.025 ± 0.001	5.5	34.7	8.3
NGC 7099	0.03	0.005 ± 0.001	0.018 ± 0.003	2.4	29.8	8.2

Cluster ID	R_V	Cluster ID	R_V
NGC 2298	3.11 ± 0.11	NGC 6352	2.36 ± 0.20
NGC 3201	3.19 ± 0.12	NGC 6366	3.70 ± 0.43
NGC 5286	2.04 ± 0.28	NGC 6388	1.92 ± 0.24
NGC 5927	2.43 ± 0.16	NGC 6441	2.60 ± 0.43
NGC 5986	4.15 ± 0.44	NGC 6496	3.53 ± 0.23
NGC 6093	3.93 ± 0.18	NGC 6535	2.32 ± 0.18
NGC 6121	3.85 ± 0.13	NGC 6541	3.40 ± 0.19
NGC 6144	1.93 ± 0.25	NGC 6656	2.53 ± 0.11
NGC 6171	3.01 ± 0.11	NGC 6779	2.87 ± 0.19
NGC 6254	3.35 ± 0.27	NGC 6838	2.36 ± 0.20
NGC 6304	2.64 ± 0.16		

Table 2. This table lists for each of the 21 highly-reddened GCs the new values of R_V with the corresponding error calculated in Section 4.

- Fitzpatrick E. L., Massa D., 1990, *ApJS*, **72**, 163
 Gonzalez O. A., Rejkuba M., Zoccali M., Valenti E., Minniti D., 2011, *A&A*, **534**, A3
 Harris W. E., 1996, *AJ*, **112**, 1487
 Heitsch F., Richtler T., 1999, *A&A*, **347**, 455
 Hendricks B., Stetson P. B., VandenBerg D. A., Dall’Ora M., 2012, *AJ*, **144**, 25
 Jang S., et al., 2022, *MNRAS*, **517**, 5687
 Kaluzny J., Krzeminski W., 1993, *MNRAS*, **264**, 785
 Lagioia E. P., et al., 2014, *ApJ*, **782**, 50
 Legnardi M. V., et al., 2022, *MNRAS*, **513**, 735
 Li C., de Grijs R., Deng L., Milone A. P., 2017, *ApJ*, **844**, 119
 McWilliam A., Zoccali M., 2010, *ApJ*, **724**, 1491
 Milone A. P., 2015, *MNRAS*, **446**, 1672
 Milone A. P., et al., 2012, *A&A*, **540**, A16
 Milone A. P., et al., 2017, *MNRAS*, **464**, 3636
 Milone A. P., et al., 2022, arXiv e-prints, p. arXiv:2212.07978
 Nardiello D., et al., 2018, *MNRAS*, **481**, 3382
 Nataf D. M., et al., 2013, *ApJ*, **769**, 88
 Nataf D. M., et al., 2016, *MNRAS*, **456**, 2692
 O’Donnell J. E., 1994, *ApJ*, **422**, 158
 Pallanca C., et al., 2021, *ApJ*, **917**, 92
 Piotto G., Zoccali M., King I. R., Djorgovski S. G., Sosin C., Rich R. M., Meylan G., 1999, *AJ*, **118**, 1727
 Piotto G., et al., 2015, *AJ*, **149**, 91
 Sabbi E., et al., 2016, *ApJS*, **222**, 11
 Sarajedini A., et al., 2007, *AJ*, **133**, 1658
 Sneden C., Gehrz R. D., Hackwell J. A., York D. G., Snow T. P., 1978, *ApJ*, **223**, 168
 Stetson P. B., Pancino E., Zoccali A., Sanna N., Monelli M., 2019, *MNRAS*, **485**, 3042
 Udalski A., 2003, *ApJ*, **590**, 284
 von Braun K., Mateo M., 2001, *AJ*, **121**, 1522

APPENDIX A: MULTIPLE POPULATIONS AND DIFFERENTIAL REDDENING

All GCs studied in this work show multiple stellar populations with different chemical compositions that define distinct sequences along the entire CMD (Milone et al. 2017). In this appendix, we investigate whether or not the presence of multiple populations in a GC affects the differential reddening determination, described in Section 3.

To do that, we first simulated the m_{F814W} versus $m_X - m_{F814W}$ CMDs, where $X=F275W$, $F336W$, $F438W$, and $F606W$, to which we have added the map of differential reddening shown in the left panel of Figure A1. In close analogy with Milone et al. (2012, see their

appendix A), the reddening variations that we simulated are related to stellar positions (X, Y) by the following relations:

$$\Delta E(B - V) = C_1(\cos X' + \sin Y') \quad (A1)$$

where

$$X' = C_2\pi(X - X_{MAX})/(X_{MAX} - X_{MIN}),$$

$$Y' = C_2\pi(Y - Y_{MAX})/(Y_{MAX} - Y_{MIN}).$$

Specifically, $X_{MIN,MAX}$ and $Y_{MIN,MAX}$ correspond to the minimum and maximum values of X and Y, respectively, whereas C_1 and C_2 are two free parameters determining how the reddening variations are distributed across the FoV of the cluster (see Milone et al. 2012 for details). We fixed $C_1 = 0.012$ and $C_2 = 2.5$ in such a way that the simulated map resembles the one of NGC 6838. This cluster, which has been widely studied in the context of multiple populations, hosts first and second-population stars with different chemical compositions. The stellar populations of NGC 6838 can be followed continuously along various evolutionary sequences, including the red horizontal branch, the RGB, the SGB, and the MS (Cordoni et al. 2020; Dondoglio et al. 2021; Legnardi et al. 2022).

To investigate the impact of multiple populations on the determination of differential reddening, we simulated two groups of CMDs. We used the same number of stars and the same $F814W$ luminosity distribution as observed in NGC 6838. We first derived CMDs where stars belong to a single population. We assumed for all stars the colours and magnitudes inferred from first-population stars by Legnardi et al. (2022). Then, we simulated CMDs composed of first- and second-population stars. In this case, second-population stars comprise 70% of the total number of stars, which is a typical value for Galactic GCs (Milone et al. 2017; Dondoglio et al. 2021). We adopted the colours and magnitudes of the two stellar populations measured by Legnardi et al. (2022).

We corrected these CMDs with the same procedure described in Section 3 obtaining a reddening map that is similar to the one that we have simulated. We assumed the differences between the measured differential-reddening values (ΔA_{F814W}^{OUT}) and the simulated ones (ΔA_{F814W}^{IN}) as an estimate of the effectiveness of the correction procedure.

Results are shown in Fig. A2 where we plotted this quantity as a function of the X coordinate for the two investigated cases, namely CMDs hosting a simple stellar population (SSP, bottom) and two stellar populations (MP, top). In both cases, we obtained a similar value for the average difference between ΔA_{F814W}^{OUT} and ΔA_{F814W}^{IN} , which is close to zero. However, we note that in the MP simulations we obtain a dispersion of the $\Delta A_{F814W}^{OUT} - \Delta A_{F814W}^{IN}$ quantity (σ) that is ~ 1.25 times higher than that derived from the simple-stellar population CMDs. We conclude that the multiple populations affect the uncertainties on differential-reddening determinations but do not introduce significant systematic errors.

This paper has been typeset from a \LaTeX file prepared by the author.

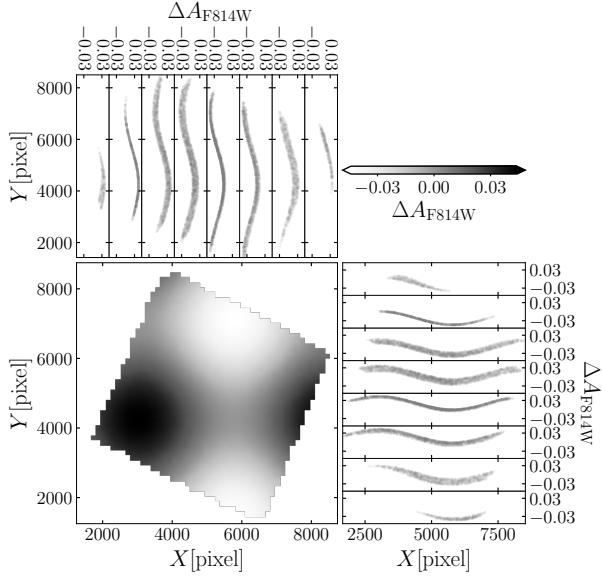


Figure A1. Differential-reddening map added to the simulated CMDs. The top and right panels show ΔA_{F814W} as a function of the X and Y coordinate of the horizontal and vertical slices in which we divided the FoV.

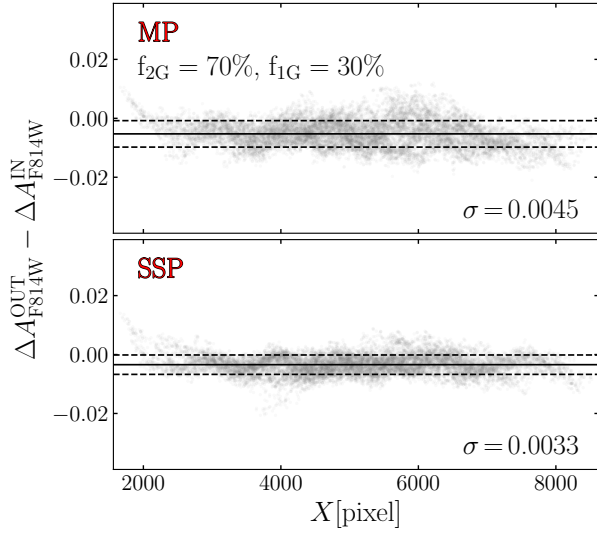


Figure A2. Difference between the measured differential-reddening values (ΔA_{F814W}^{OUT}) and the values of differential reddening used in the simulation (ΔA_{F814W}^{IN}) as a function of the X coordinates. The black continuous line marks the average difference, whereas the dashed lines are indicative of the dispersion of the residuals. We show the results in the case of a simulation of a GC with two stellar populations (top) and a single stellar population (bottom).